Research article

Incorporating multi-source remote sensing in the detection of earthquake-damaged buildings based on logistic regression modelling

Qiang Li [*], Jingfa Zhang, Hongbo Jiang

National Institute of Natural Hazards, Ministry of Emergency, Beijing, No. 1 Anning Zhuang Road, Xisanqi, Haidian District, 100085, China

A B S T R A C T

After an earthquake, efficiently and accurately acquiring information about damaged buildings can help reduce casualties. Earth observation data have been widely used to map affected areas after earthquakes. However, fine post-earthquake assessment results are needed to manage recovery and reconstruction and to estimate economic losses. In this paper, for quantification and precision purposes, a method of earthquake-induced building damage information extraction incorporating multi-source remote sensing data is proposed. The method consists of three steps : (1) Analysis of multisource features that describe texture, colour, and geometry, (2) rough set theory is carried out to further determine the feature parameters, (3) Logistic regression model (LRM) was built to describe the relationship between the occurrence and absence of destroyed buildings within an individual object. Old Beichuan County (centered at approximately 31.833 °N, 104.459° E), China, the area most devastated by the Wenchuan earthquake on May 12, 2008, is used to test the proposed hypothesis. Multi-source remote sensing imagery include optical data, synthetic aperture radar (SAR) data, and digital surface model (DSM) data generated by interpolating light detection and ranging (LiDAR) point cloud data. Through comparison with the ground survey, the experimental results show that the detection accuracy of the proposed method is 94.2 %; the area under the receiver operating characteristic (ROC) curve is 0.827. The efficiency of the proposed method is demonstrated using 6 modes of data combination acquired from the same area in old Beichuan County. The approach is one of the first attempts to extract damaged buildings through the fusion of three types of data with different features. The approach addresses multivariate regression methodologies and compares the potential of features for application in the damage detection field.

1. Introduction

Earthquake disasters are a type of major natural disaster, and severe earthquakes can cause serious casualties and economic losses through the destruction of the local area [1,2]. After an earthquake, quickly and accurately obtaining information about the disaster distribution to improve rescue work efficiency is an effective way to reduce losses [3–5]. Building damage can reflect the intensity of the ground motion and the economic losses to a certain extent. Quantitative evaluation and fine building assessment can also provide important information regarding economic loss, which can be used to allocate resources during restoration and reconstruction [6,7]. Therefore, quantitatively evaluating the earthquake damage of buildings is vital [8].

Remote sensing technology is an important way to obtain information in the early stage of earthquake relief because of its objective and efficient access to a wide range of disaster information, which can provide information to support earthquake damage assessment and emergency rescue [9,10]. Notably, with the continuous development of satellite technology, the number of satellites operating in orbit and sensors are increasing, and a large amount of remote sensing data can be acquired after a disaster. Most remote sensing data used after a disaster can be classified into three categories: (1) optical data, (2) synthetic aperture radar (SAR) data, and (3) light

* Corresponding author.
   E-mail address: liqiang08@163.com (Q. Li).

detection and ranging (LiDAR) data. Building damage information extraction is the main task of earthquake damage information investigation [11,12]. There are many works in the literature on this topic that consider both optical and radar data for different earthquakes. In Table 1, we have reviewed the literature of scholars in the past 30 years on identifying earthquake damaged buildings using multi-source remote sensing images after many earthquakes, such as Santomena Earthquake, Kobe Earthquake, and Izmit Earthquake. It can be found that in the early stages, single data was mainly used for extracting earthquake damaged buildings, especially drone images. Later, with the improvement of SAR image resolution, SAR images were gradually introduced into the research of earthquake damaged building identification. Early earthquake damage identification mainly relied on high-resolution optical and SAR images, with relatively limited research on multi-source remote sensing images. However, earthquake-damaged buildings is complex and variable, and comprehensively identifying seismic information by relying on a single data source is difficult. With the rapid development of space and airborne remote sensing technology, obtaining different types of remote sensing data within a short period after an earthquake is possible. The effective combination of multi-source data can make full use of the respective advantages of these data to achieve complementary advantages and redundant control. As for the approaches of multisource remote sensing data fusion, the widely used methods mainly include feature-level fusion and decision-level fusion. Specifically, in the procedure of feature-level fusion, remote sensing data from different sources are firstly processed to extract the relevant features and then fused through feature stacking or feature reconstructing. Butenuth et al. comprehensively used multi-source remote sensing data to extract road damage information and achieved good results, which indicates its validity in earthquake damage information identification [13]. Chini et al. investigated the 2011 Tohoku tsunami inundation and liquefaction through a combination of optical data, thematic maps, and SAR data [14]. Wang and Jin proposed a method for identifying seismic damage through the combination of IKONOS, COSMO-SkyMed, and Radarsat-2 images after an earthquake. First, the SAR image before the earthquake was simulated using the geometric information extracted from the optical image. Then, the simulated image was compared with the real image after the earthquake to extract the building damage information; the extraction accuracy reached 85 % [15]. These authors believed that the combination of optical and SAR images can effectively improve the extraction accuracy and found that the optical image can be used to identify destroyed buildings. SAR image texture features can be used to identify seismic damage information in blocks. The complexity of the image-forming mechanisms within an earthquake region, especially for radar images, makes the interpretation and analysis of images a challenging task. In particular, discrimination of geometric features is extremely difficult in the fine identification of earthquake-damaged buildings.

In addition to the combination of optical and SAR images, the combination of optical and LiDAR images has also made some progress. The integration is mainly based on the texture features of optical data and the elevation information of LiDAR data. Rehor and Voegtle improved the previous method of extracting buildings by the fusion of optical and LiDAR images. In addition, optimal texture features are used in the calculation [66]. Compared with the single use of optical images and LiDAR images, the accuracy is improved when these images are combined. Based on the object-oriented support vector machine method, Yu et al. extracted the information of damaged buildings through the combination of the digital surface model (DSM) obtained from aerial and LiDAR data. LiDAR data and high-resolution images were used to reconstruct the 3D building model; then, the roof of the building model was compared with the pre- and post-earthquake roof patches to quantify the degree of damage to the building [67]. Hussain et al. detected the ruins of collapsed houses in the Port Au Prince area using the GeoEye-1 and LiDAR data after Haiti Earthquake [68]. Through this method, the volume of rubble and debris can be estimated, and the cleaning process can be planned effectively. The features of two types of data are not enough to identify different types of buildings completely. However, there are no data fusion approaches for multi-source remote sensing data in the existing research [69].

Nevertheless, the above studies have two drawbacks that could be improved. Firstly, the data-fusion method of simply stacking or concatenating different features does not consider the importance or contribution of each feature to the final extraction task, which could be improved by assigning a specific weight to each feature. Secondly, the data fusion method have not truly achieved deep feature fusion, but rather the combination and application of features. To tackle these problems, this paper presents a quantitative evaluation method for earthquake-damaged buildings based on multi-source remote sensing data, including optical images, SAR images, and LiDAR images. Two specific aspects of this work are deemed important for satisfying the final needs of complete and

Table 1

Research workers on earthquake damage information extraction in the literature for different earthquakes.

Earthquake	Occurrence time	Research worker	Data
Santomena earthquake	1980	[16]	Aerial photographs
Kobe Earthquake	1995	[17,18]	Aerial photographs , SAR
Izmit Earthquake	1999	[19–21]	Aerial photographs, VHR optical and SAR image
Nantou earthquake	1999	[22]	SAR
Bam earthquake	2003	[23–35]	VHR optical and SAR image
Boumirdas earthquake	2003	[36–39]	VHR optical and SAR image
Indonesia earthquake	2004	[40]	SAR image
Kashmir earthquake	2005	[41]	VHR optical image
Java earthquake	2006	[42–45]	VHR optical and SAR image
Peru earthquake	2007	[46]	SAR
WenChuan Earthquake	2008	[47–55]	VHR optical and SAR image, airborne image
L'Aquila earthquake	2009	[56,57]	VHR SAR image
haiti earthquake	2010	[58–63]	VHR optical and SAR image, Airborne oblique Pictometry
Sendai earthquake	2011	[64,65]	Airborne SAR, VHR SAR image

detailed inventories and for ensuring that this work can provide a reliable product (i.e., the damage map, in our case). The first important aspect is a fine assessment comparison with the rapid assessment of single image data, which provides a well-known and reliable decision-making reference. The second aspect is that the work is not just an exercise in collapse detection focused on a few buildings, but rather an evaluation of the capability of multi-source remote sensing in the quantitative assessment of earthquake-damaged buildings, which is important for assessing the role of earth observation in earthquake damage management with respect to methodological testing on a limited test set. The paper is structured as follows. Section 2 introduces the study area and three different datasets. Section 3 describes the characteristics of buildings with different types of earthquake damage in multi-source remote sensing images. The proposed methodologies regarding feature selection, attribute reduction, element determination, and logistic regression model (LRM) are introduced in Section 4. Section 5 presents the results of the experiment and discusses the feasibility of the method. Finally, Section 6 presents the main conclusions.

2. Study case and datasets

Old Beichuan County is regarded as the study area in this paper. The area of Old Beichuan County is 2.66 Km^2. MS 8.0 Wenchuan earthquake caused Beichuan County massive destruction, and resulted in casualties more than ten thousand (Linsulted. The whole Beichuan County has become in ruins. Field seismic investigation showed that the three principal causes of such huge destruction are as follows: (1)the vibration failure effect caused by macroseism vibration; (2) the earth's surface rupture effect caused by seismo-active fault slippage; and (3) the secondary geological hazards (collapse, landslide and debris flow) caused by the earthquake [70,71].

Many buildings have been preserved in the form of earthquake memorials. The buildings in the Memorial Park retain their damaged post-earthquake appearance [72]; thus, they can be used as the research object of this paper.

The datasets applied in this work include optical multispectral image, LiDAR, and SAR images. In July 2013, the Institute of Crustal Dynamics, China Earthquake Administration carried out a series of unmanned aerial vehicle (UAV) multispectral images from the Wenchuan earthquake site, including old Beichuan County. The resolution of the images is approximately 0.5 m. The optical image we obtained was then rectified. In the same year, we carried out the omni-directional scan on the site of the old town in Beichuan using the ground laser scanner. A total of 67 station sites were laid in old Beichuan County. In 2014, we carried out additional measurements on old Beichuan. In addition, field investigation data of earthquake damage to buildings were obtained. The SAR image is TerraSAR-X data taken from the German Aerospace Center (DLR). The data are ascending SAR images in VV polarization mode. The spatial resolution is 1 m. The information of the datasets used in the experiments is shown in Table 2.

Combining the careful interpretation of multi-source images and field investigation data, we can obtain a reference map divided into intact buildings and destroyed buildings. Due to the lack of detailed field survey data, the reference map can be regarded as the ground truth information for accuracy verification. The study area location is showm in Fig. 1. The optical image acquired in 2013 using UAV is Fig. 1(a) and (b) is the building distribution acquired by the high-resolution optical image interpretation and field investigation. Fig. 2 presents the multi-source remote sensing images of the study area (Fig. 2(a)), SAR image (Fig. 2(b)) and DSM image (Fig. 2(c)).

3. Seismic characteristics of multi-source remote sensing images

The destruction of buildings during an earthquake is complex and diverse. Schweier and Markus divided the types of building damage into 10 categories, including plane tilt, multi-layer collapse, debris accumulation, and wall tilt. Different sources of remote sensing data reflect different properties [73]. Therefore, the quality of different types of seismic damage in the images also varies.

Generally, the buildings in the optical image are in perfect shape before the earthquake, and the body and shadow of a building are shown as morphological rules and boundaries [74–76]; SAR image contains an overlapping area, a reflection area, a roof area, and a shadow area [77–79]. From the perspective of the characteristics of radar images, intact buildings show a relatively regular arrangement [80–82]; the spatial relationship between each characteristic is in accordance with the characteristics of the building complex. Due to the characteristics of SAR side view imaging, in close range, the first characteristic is the overlay area of the wall, which is higher than the surface in the image; hereafter, the wall and surface reflection effect and the dihedral angle of the back-scattering intensity on one side of the building are high and show 1- or L-shaped strong echo characteristics. Moreover, the strong echo location is still consistent with the arrangement of the buildings. In the direction from back to incident, a clear rectangular shadow area can be seen [83]. In the LiDAR image, the three-dimensional structure of the building is clear and complete, and the columns and walls are not obviously missing or tilting. The walls, columns, and ground are at right angles. The wall is smooth and complete [84]. The point cloud echo is dense.

After the building was destroyed, the square feature was obviously damaged or disappeared in the optical image. The boundaries of the building are all blurred, or the buildings are level with the surrounding surface. The roof of the building collapsed and broke into

Table 2
The information of the datasets used in the experiments.

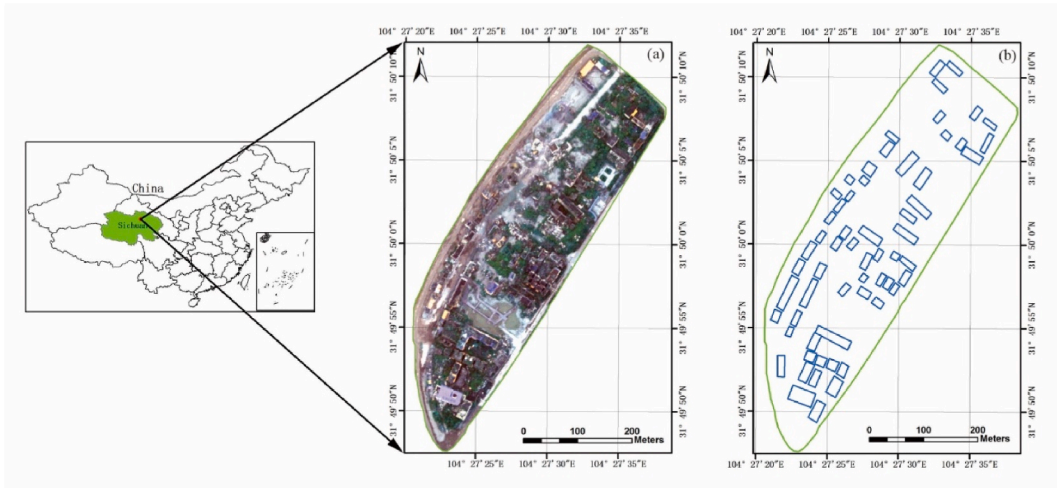| Datasets	Acquisition time	Spatial resolution
UAV optical multispectral image	2013.10	0.25 m
Ground-based LiDAR	2013.10	0.5 m
SAR (TerraSAR)	2014.5	1 m

Fig. 1. Study area. (a) Geographical location of the study area and the optical image acquired in 2013 using UAV; (b) the building distribution acquired by the high-resolution optical image interpretation and field investigation.
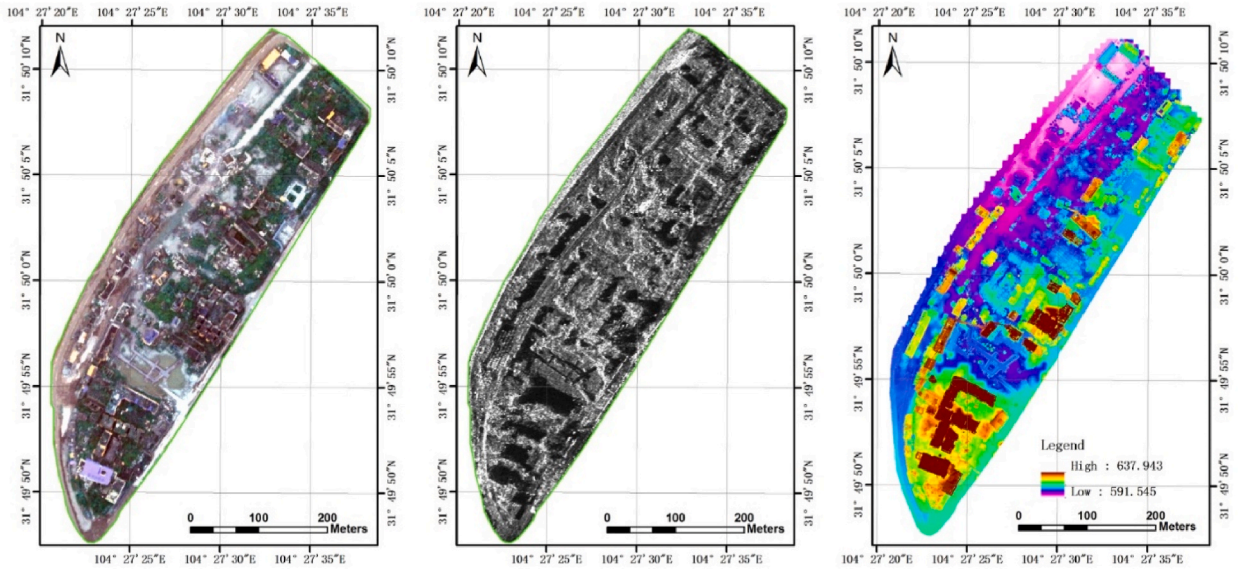

Fig. 2. Multi-source remote sensing image of the study area. (a) Airborne multispectral remote sensing image acquired on July 4, 2013; (b) TerraSAR-X ascending image acquired on December 4, 2014 (the azimuth direction is from bottom to top, and the range direction is from left to right); and (c) DSM image generated with the LiDAR point cloud data interpolation, the data was acquired on July 20, 2014.
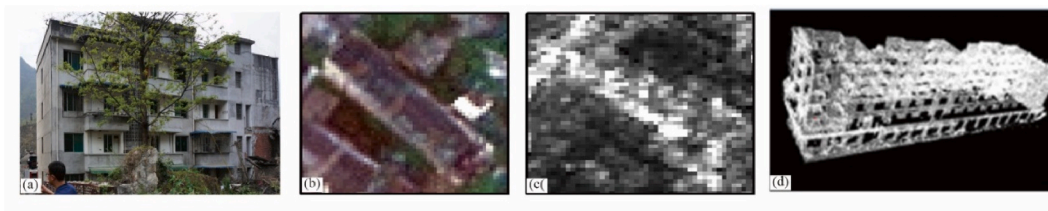

Fig. 3. Intact building after the earthquake (centered at approximately 104.46°E and 31.83°N) : (a) Field investigation photograph; (b) optical image acquired in 2013; (c) TerraSAR-X ascending image (the azimuth direction is from bottom to top, and the range direction is from left to right); and (d) LiDAR image acquired in 2013.

pieces. The shadow cannot be clearly identified because of the rubble. The whole building was broken down, collapsed, or slumped. The original geometric structure in the SAR image is blurred or even absent, and the backscattering pattern is changed to multiple scatters in all directions [85]. The main rule of image recognition is that the image brightness is high, and no regular bright spot occurs in a certain position. In the LiDAR image, the three-dimensional shape of the building is completely absent and in ruins. A large number of peeling walls and reinforcements are present in the middle of and surrounding the building [86].

Fig. 3 illustrates an intact building (centered at approximately 104.46°E and 31.83°N) obtained from different sensors after the earthquake and field investigation photograph (Fig. 3(a)). In the optical image (Fig. 3(b)), the shape is regular, the colour is even, and no abrupt changes occur. From Fig. 3(c), we can distinguish clearly the double-bounce line, layover area, and shadow area. The lateral and horizontal roof of the building result in the formation of black areas. In the LiDAR image (Fig. 3(d)), the three-dimensional structure is clear, and the wall is smooth and complete.

Fig. 4 illustrates the destroyed building after the earthquake (centered at approximately 104.45°E and 31.84°N) obtained from different sensors and field investigation photograph (Fig. 4(a)). In the optical image (Fig. 4(b)), the geometry is completely absent, the ground is covered with the rubble from the building, and differences in brightness are present. In the SAR image (Fig. 4(c)), the area of the building where the echo signal is poor contains dark colors, overlapping objects, bright lines formed by angle reflections, and shadows and missing features. A small corner reflector is formed locally by rubble, so there are many highlights. In the LiDAR image (Fig. 4(d)), the three-dimensional shape of the building is completely missing and in ruins. A large number of peeling walls and steel can be found in the middle of and surrounding the building.

Figs. 3 and 4 show that intact buildings and destroyed buildings have unique features in the optical images, SAR images, and LiDAR images. However, in the optical images, the characteristics of the construction ruins and the ruins of destroyed buildings are similar; additionally, phenomena of "same object with different spectra, different objects with the same spectrum or different optical image spectra, and objects with the same spectrum" occur. The characteristics of large amounts of vegetation in the SAR images appear similar to those of completely destroyed buildings. The method of information extraction based on a single data source can easily cause false alarms. Using traditional methods to achieve high-precision extraction of buildings with different types of seismic damage is difficult. Therefore, the motivation of this paper is to make full use of the characteristics of multi-source remote sensing data and establish a quantitative evaluation model.

4. Methodology

Based on the above analysis, buildings with different degrees of earthquake damage can be identified through the comprehensive utilization of multi-source images. Therefore, if the features are selected and the mathematical evaluation model is constructed, then intact buildings and damaged buildings can be quantitatively evaluated. Considering this theory, in this paper, a new approach for detecting earthquake-damaged buildings using post-event multi-source remote sensing images is proposed. The approach includes the following steps: (i) Data processing, including optical image, SAR image, DSM image, and building sample distribution, (ii) Feature selection, including the spectral features of optical images, the texture features of SAR images and the geometric features of DSM images, (iii) Logistic regression Model construction and analysis. A technical flowchart of the proposed methodology is shown in Fig. 5.

4.1. Data processing

The main inputs of the method are the optical image, SAR image, DSM image, and building sample distribution. Before the feature selection of SAR data, radar sigma naught values can be obtained by Equation (1) using the original digital numbers [87]:

$$\sigma^0 = \left(k_s \cdot |DN|^2 - NEBN \right) \cdot \sin \theta_{loc} \tag{1}$$

Where σ^0 is the radar cross-sectional area (i.e. backscattering coefficient) per unit area, which can be used to characterize the scattering ability of the target to electromagnetic waves. k_s is the calibration and processor scaling factor, DN is the pixel intensity value, and NEBN is the Noise Equivalent Beta Naught, and θ_{loc} is the local incidence angle.

The optical image is a UAV image with a resolution of approximately 0.2 m. The DSM image is generated by the nearest neighbor interpolation method of the Ground LiDAR Point Cloud Data collected using the VZ-1000 3D laser scanning system of Austria Riegle
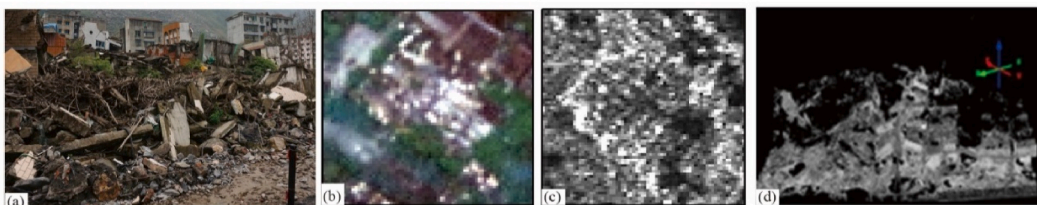

Fig. 4. Destroyed building after the earthquake (centered at approximately 104.45°E and 31.84°N) . (a) Field investigation photograph; (b) optical image acquired in 2013; (c) TerraSAR-X ascending image (the azimuth direction is from bottom to top, and the range direction is from left to right); and (d) LiDAR image acquired in 2013.
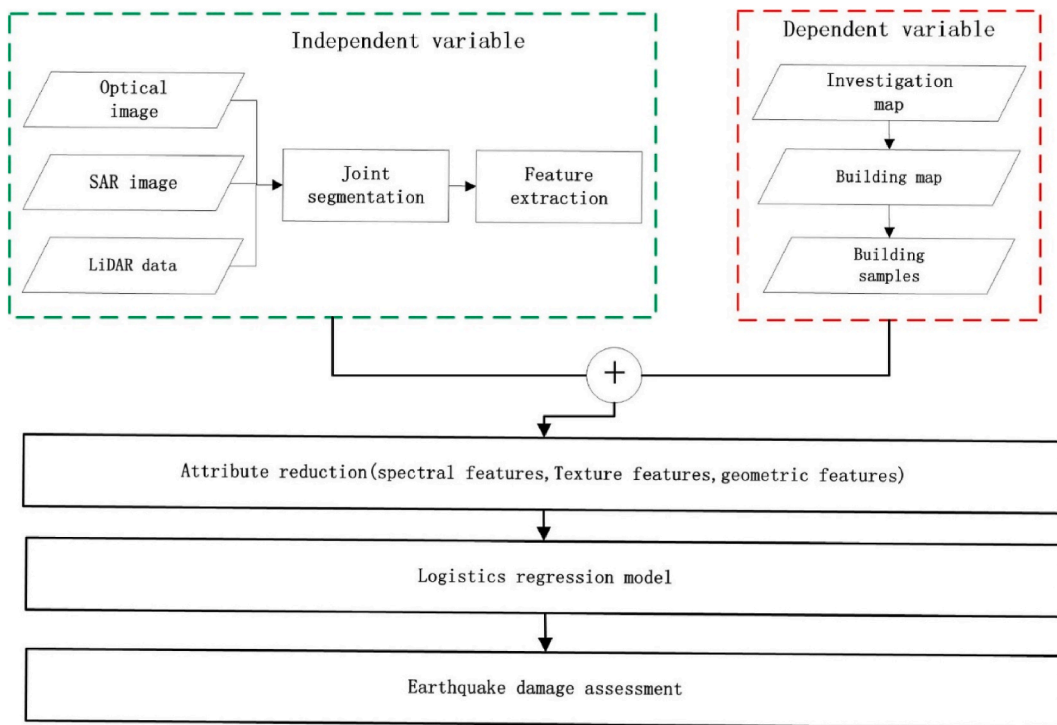
Fig. 5. Technical flow of the proposed methodology.

Company.

The building distribution map is obtained by carefully interpreting the post-earthquake optical image, LiDAR data, and field investigation data through comparison with the Google-earth image. To carry out this comparative analysis effectively, the optical image, SAR image, and DSM image are corrected using the manual control point selection function implemented into ENVI software. Subsequently, the distribution of buildings can be determined in the three types of images.

4.2. Feature selection

Three different types of image features are selected for our experiments, including the spectral features of optical images, texture features of SAR images and the geometric features of DSM images. The spectral feature is the most intuitive representation of different objects in optical images. The features mainly include maximum (MAX), mean value of spectral features (MES), standard deviation (SD), and brightness (BR). For the detailed calculation process, refer to the relevant reference [88].

The repeated occurrence of pixel intensity in the spatial position forms the texture of the image. A difference in the spatial arrangement of pixel intensity is expected as a consequence of damage. In particular, features based on second-order statistics are considered in SAR images obtained from the grey-level co-occurrence matrix (GLCM) method using ENVI software, following the approach proposed by Haralick et al. [89]. Taking four angular directions ($0°$, $45°$, $90°$, $135°$), a step size d = 1 and the window size w = 11, four different variables were calculated, and the average is obtained by summing them. From the results of GLCM, eight texture features, i.e., mean value of texture features (MET), variance (VA), homogeneity (HOM), contrast (CON), dissimilarity (DIS), entropy (ENT), angular second moment (ASM), and correlation (COR), are chosen for analysis. The features are as follows [90].

In addition to elevation (ELE) information, the main feature of the DSM image is the geometric feature. The geometric feature is the spatial distribution of the pixels. The covariance matrix is used to carry out statistical analysis [91]:

$$S = \begin{bmatrix} \text{Var}(X) & \text{Cov}(XY) \\ \text{Cov}(XY) & \text{Var}(Y) \end{bmatrix} \tag{2}$$

In Eq. (2), X represents the x coordinates of all pixels in the image object, Y represents the y coordinates of all pixels in the image object, Var(X) and Var(Y) represent the variance of X and Y, respectively, and Cov(XY) represents covariance (COV). Length-width ratio (LWR), shape index (SPI), density (DEN), compactness (COM), asymmetry (ASY), and rectangularity (REC) are adopted in our experiment. Notably, length-width ratio refers to the proportion of the height and width of the segmentation object. SPI describes the smoothness of the image object border. The smoother the boundary, the lower SPI. DEN describes the distribution in the pixel space of an image object. The "densest" shape is a square; the more objects resemble filaments, the less dense they are. COM describes the compactness of image objects; it is similar to the boundary index but based on area. The tighter the image object is, the smaller the

border. ASY describes the relative length of an image object compared with a normal polygon. An ellipse is similar to a given image object, and it can be expressed by the ratio of the length of its small axis to that of its large axis. The eigenvalues increase with ASY.

There are many characteristics of seismic damage in multi-source remote sensing images; thus, we should consider as many features as possible. However, the correlation between some factor characteristics and performances and the causal relationship of earthquakes is not large, and including these factors results in redundant data and makes the task onerous and meaningless. Therefore, selecting as few factors as possible is necessary while also determining which factors best characterize the buildings. Rough set theory is used to reduce the features in our experiment. Rough set theory was put forward in the early 1980s by Pawlak Z, who is an expert at the University of Warsaw in Poland and is mainly used to study the learning, expression, and induction of incomplete data and imprecise knowledge [92–95]. A rough set is used to delete irrelevant or unimportant redundant data, and then knowledge discovery and mining is carried out on the premise of maintaining the ability to generalize the knowledge base. The most important feature of rough set is that it can provide core knowledge of the data and reduce the complexity of the spatial cognition of a complex system.

4.3. LRM construction and analysis

An appropriate model element is the basis of the spatial assessment of earthquake damage to buildings and has an important influence on the evaluation results. In our experiment, multi-resolution segmentation is used to obtain the model element. Multiscale segmentation is a bottom-up approach and is achieved by merging adjacent pixels or small segmented objects under the premise that the average heterogeneity between the objects is the smallest and the homogeneity of the inner pixels is the largest [96]. Multiscale segmentation has been widely used in different types of image segmentation.

To obtain image objects of the same size, we use the multi-data joint segmentation strategy. The image segmentation scale is set to 60. Due to interference factors, there are some differences between the object range and the range of the building, and a method of comparing the building area with the image object is proposed in this paper. When 2/3 of the area of an image object is located in the position of a building, the object is considered a building; when the area is less than 2/3, the image object is excluded.

Based on the above content preparation, we can build a logistic regression model. Logistic regression analysis is a statistical analysis method for the two categorical dependent variables (the dependent variable y takes only two values: 1 and 0 or yes and no) [97,98]. The probability Equation of destroyed buildings and intact buildings using logistic regression is as follows [99]:

$$P = \frac{e^{a+b_1x_1+b_2x_2+\dots+b_nx_n}}{1 + e^{a+b_1x_1+b_2x_2+\dots+b_nx_n}} \tag{3}$$
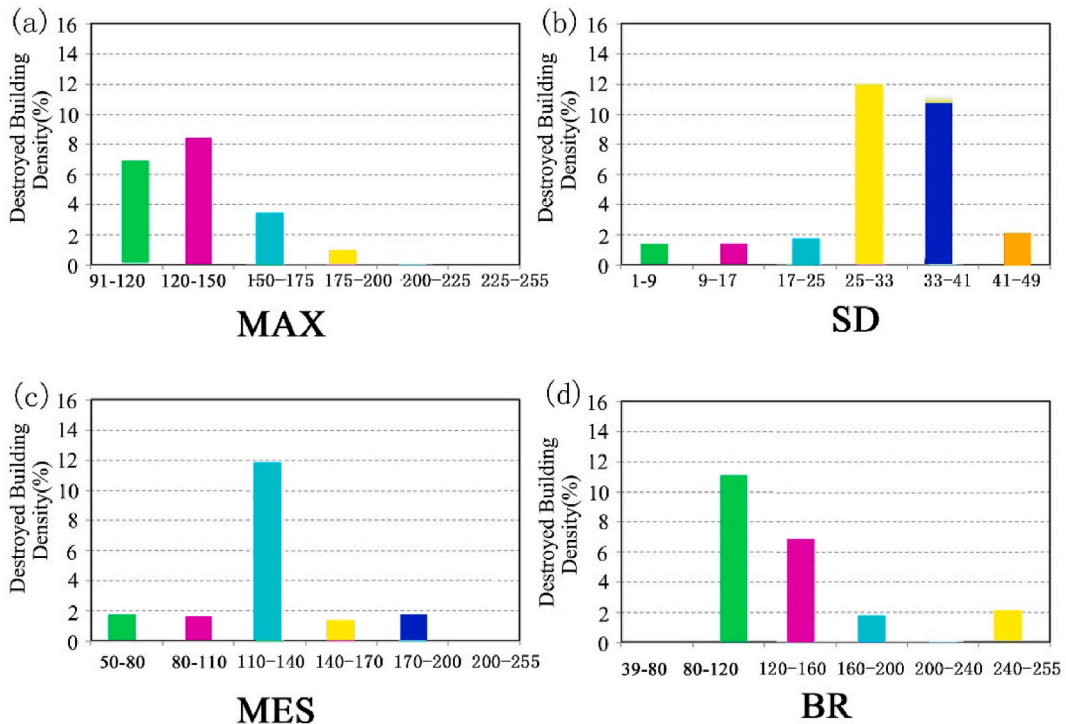

Fig. 6. Density distribution of destroyed buildings with different spectral feature. (a) Is the Maximum (MAX) value of spectral features. (b) Is the standard deviation (SD) value of spectral features; (c) is the mean value of spectral features (MES); and (d) is the brightness (BR) value of spectral features. Different colors indicate the density of destroyed buildings in different abscissa.

$$Q = \frac{1}{1 + e^{a + b_1 x_1 + b_2 x_2 + \ldots + b_n x_n}} \tag{4}$$

Where, P represents the probability of destroyed buildings and Q represents the probability of intact buildings. $x_1, x_2, \ldots x_n$ represents the N features of multi-source remote sensing images. a is a constant and $b_1, b_2, \ldots b_n$ are the logistic regression coefficients.

The relationship between the probability of occurrence of an event and the influencing factors is obtained via comparison between Eq. (3) and Eq. (4). Eq. (3) is divided by Eq. (4) and then taken as the natural logarithm, afterwards, Eq (5) can be obtained

$$\ln\left(\frac{P}{Q}\right) = f(x) = a + b_1 x_1 + b_2 x_2 + \ldots + b_n x_n \tag{5}$$

The logistic regression analysis method can be used to establish the quantitative evaluation model. The probability P is used as the earthquake damage assessment index (EDAI) to evaluate the ability of a feature factor $x_1, x_2, \ldots x_n$ to represent whether buildings are destroyed. Then, the spatial distribution of seismic damage in buildings is evaluated. The Statistical Package of Social Sciences (SPSS) is used to determine the relationship between calculated factors and buildings with different damage degrees.

5. Results and discussion

5.1. Features statistics and analysis

We selected 18 feature factors to construct the regression analysis model. The feature factors are calculated by the eCognition software. Prior to the calculation, the spatial resolution of the three types of remote sensing images in the study area are resampled to 1 m using the nearest neighbor method. The image of the study area contains 548 columns and 889 rows, and the number of pixels is 487172.

The spectral features are mainly aimed at the optical image, including MAX, MES, BR, and SD. Each eigenvalue is divided into 6
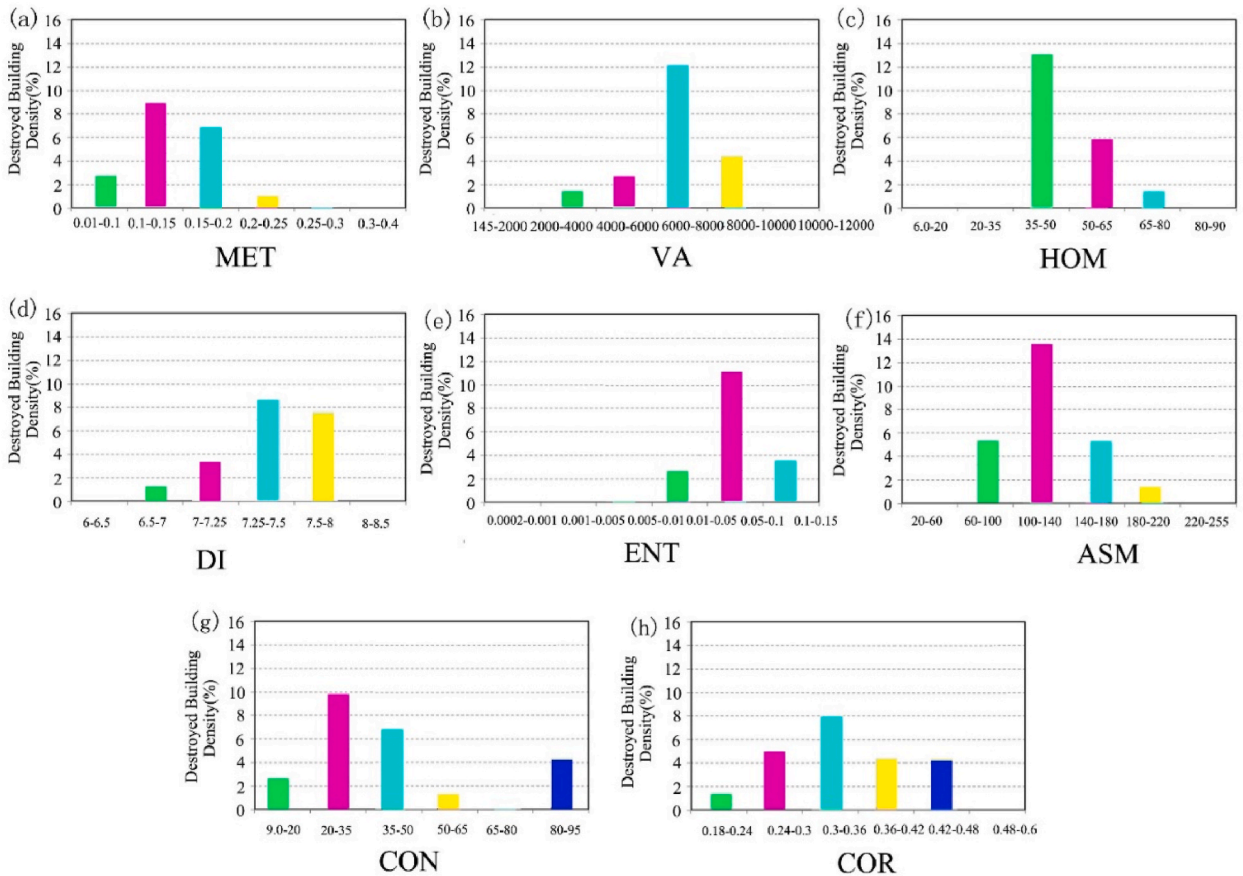

Fig. 7. Density distribution of destroyed buildings with different texture features: (a) is the mean value of texture features (MET). (b) Is the variance (VA) value of texture features. (c) Is the homogeneity (HOM) value of texture features. (d) Is the dissimilarity (DI) value of texture features. (e) Is the entropy (ENT) value of texture features. (f) Is the angular second moment (ASM) value of texture features. (g) Is the contrast (CON) value of texture features. and (h) is the correlation (COR) value of texture features. Different colors indicate the density of destroyed buildings in different abscissa.

categories to calculate the percentage of destroyed building pixels in each category. Fig. 6(a)-Fig. 6(d) illustrate the distribution of destroyed building pixels in each of the features. In the MAX value distribution (Fig. 6(a)), more than 15 % of the destroyed buildings are mainly distributed between 91 and 150. In the MES value distribution (Fig. 6(c)), 12 % of the buildings are mainly distributed between 110 and 140. In the BR value distribution (Fig. 6(d)), the destroyed buildings are mainly distributed in the range from 80 to 160. The value of the BR is low, which is consistent with the performance of the destroyed building in the optical image.

The texture features are mainly aimed at the SAR image. Considering factors such as the image resolution and the distribution of earthquake-damaged buildingsearthquake-damaged buildings, the features of this experiment include MET, COV, HOM, dissimilarity, ENT, ASM, correlation, and contrast.

Fig. 7(a)-Fig. 7(h) illustrate the density distribution of destroyed buildings with different textures. When the mean value of the two-order moment is 0.1–0.2, the density of the destroyed building is the largest and can reach 15 %. The distribution density of earthquake-damaged buildings can reach 12 % when the covariance is located in the range from 6000 to 8000. In the homogeneous image, the destroyed buildings are mainly distributed in the range from 35 to 50. In the dissimilarity image, all the buildings are distributed in the range from 0.01 to 0.15, and the highest proportion is located in the range from 0.05 to 0.1; the proportion is approximately 11 %. In the ASM image, destroyed buildings are mainly distributed in the range from 100 to 140. In the contrast image, destroyed buildings are mainly distributed in the range from 20 to 30. In the correlation image, the distribution density of destroyed buildings increases with increasing correlation and reaches the highest value at 0.3–0.36. Subsequently, the density gradually decreased.

Geometric features are the most direct physical attribute of targets. The unit we analyze geometric features is the object. It usually contains the area, perimeter and other information of the targets. The geometric features are mainly aimed at the DSM image. The features include ELE, LWR, SPI, DEN, ASY, and REC. Fig. 8 illustrates the density distribution of buildings with different geometric features. Fig. 8(a) shows that the density distribution of earthquake-damaged buildings decreases with an increasing LWR. When the aspect ratio is 1.1–1.5, which is approximately 8 %, the density is the largest. Fig. 8(b) illustrates that the destroyed building density is the largest when the SPI is in the range from 5.0 to 6, which is approximately 10.8 %. Fig. 8(c) illustrates that the density of earthquake-damaged buildings decreases with increasing DEN. In the range from 0.39 to 1.2, the density is up to 10 %. Fig. 8(d) illustrates that, when the ASY is small (0–0.015), the distribution density of the buildings is the largest. Fig. 8(e) illustrates that the distribution density of earthquake-damaged buildings is the largest when the REC value is in the range from 0.1 to 0.4. Fig. 8(f) illustrates that the buildings are mainly distributed at low ELE. At a height range from 590 to 600 m, the density of destroyed buildings reaches 12.3 %, which is consistent with the change in the height after the building is destroyed.

After segmentation, the study area is divided into 1032 object units. The corresponding attribute of the 18 feature factors and the decision attribute corresponding to the damage of the building (1 represents a destroyed building, and 0 represents an intact building) form a two-dimensional table. In the table, each row describes an object and corresponds to the features of the corresponding object; that is, the two-dimensional table contains 1032 rows and 19 columns. The initial decision table is formed by the random sampling of a 10 % table. The reduced set of spatial variations in earthquake-damaged buildings is calculated using a random sample. Fig. 9 illustrates the number of different factors in the reduction. The more times the factor appears, the greater the correlation between the
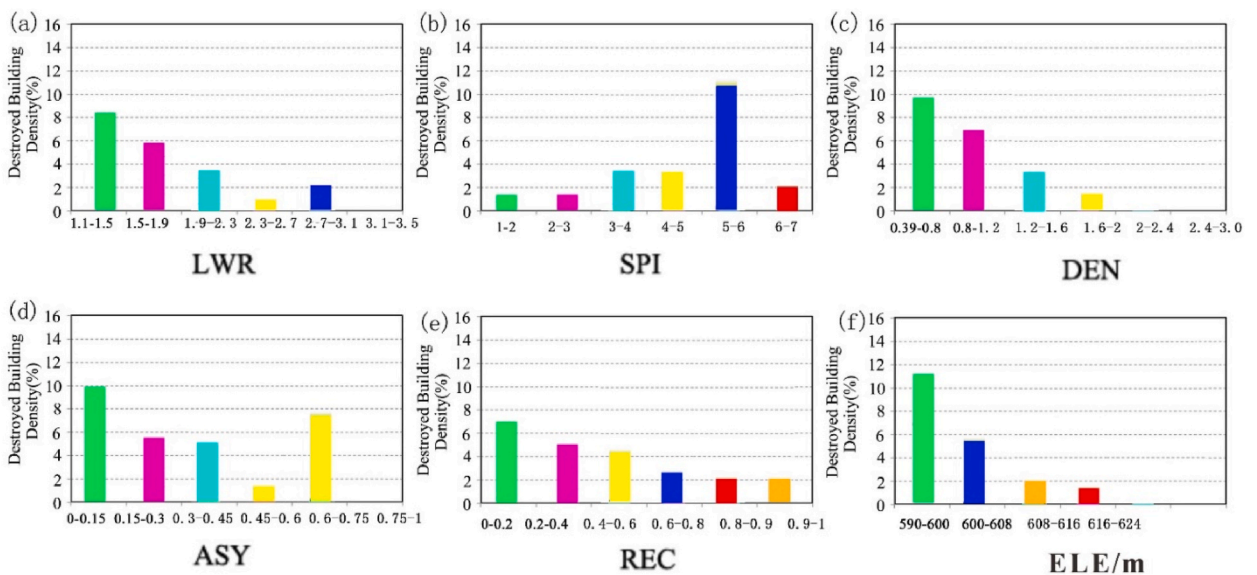

Fig. 8. Density distribution of destroyed buildings with different geometry features: (a) is the length-width ratio (LWR) value of geometry features. (b) Is the shape index (SPI) value of geometry features. (c) Is the density (DEN) value of geometry features. (d) Is the asymmetry (ASY) value of geometry features. (e) Is the rectangularity (REC) value of geometry features. and (f) is the elevation (ELE) value of geometry features. Different colors indicate the density of destroyed buildings in different abscissa.

factor attribute and the earthquake damage. We remove the 11 attributes that appear less frequently in the reduction set and obtain a feature set consisting of 7 feature factors in our experiment. Attribute reduction is calculated by using RSES software.

5.2. Identification model construction

Before the main statistical analyses, data must be normalized to eliminate the effects of different data dimensions [100]. In this study, we use a standardized processing approach to convert the value of the characteristic factor to the range from −1 to 1. The sample size is also an important factor in model construction. Generally, using similar proportions of 1 ("destroyed building") and 0 ("intact building") cells is recommended. Hence, we took 56 random samples consisting of 26 destroyed building cells and 30 intact building cells (Fig. 10).

To avoid the multicollinearity problem between explanatory variables, the stepwise method called Wald was selected [101]. We then performed entry testing based on the significance of the score statistics. The logistic regression mathematical equations were formulated using all factors. The statistical significance of each coefficient in the model is listed in Table 3. Thus, we obtained Eq (6):

$$f(x) = 1.093 \cdot BR + 0.419 \cdot CON + 0.027 \cdot ASM + 0.076 \cdot ELE + 0.183 \cdot ASY + 0.960 \cdot HOM + 0.868 \cdot SPI - 5.291 \qquad (6)$$

$f(x)$ represents the degree of earthquake damage for each object. *BR*, *CON*, *ASM*, *ELE*, *ASY*, *HOM* and *SPI* reprents brightness of spectral features, contrast, angular second moment, and homogeneity of texture features, elevation, asymmetry, and shape index of geometric features respectively.

5.3. Results and verification

To verify the validity of the method proposed in this paper, we analyze different data combinations in accordance with the technological process. The compound types are as follows: (1) Optical image, (2) SAR image, (3) DSM image, (4) Optical image + SAR image, (5) Optical image + DSM image, and (6) SAR image + DSM image.

The fitting degree of different models is compared and analyzed using Hosmer–Lemeshow Chi-square , −2 log-likelihood and Cox and Snell R Square. The overall statistics of these models are shown in Table 4. The Hosmer–Lemeshow Chi-square index, which is an important index for evaluating the goodness of fit of the model, is obtained by calculating the difference between the observed and predicted values of the dependent variable [102], 103. The smaller the value is, the better the model fits. The greater the value of the −2 log-likelihood is, the better the correlation between the selected feature factors and the assessment events. The greater the value is, the higher the Cox and Snell R Square value, and the better the performance of the model.

(1) Quantitative analysis of evaluation precision

Receiver operating characteristic (ROC) analysis is used to summarize the performance of the LRM. ROC, which is a comprehensive index reflecting sensitivity and specificity, is a method used to reveal the relationship between sensitivity and the proportion of false negatives [104]. The area under the ROC curve indicates the accuracy of the model. Theoretically, the measure has a value from 0.5 to 1. When the value is 1, the evaluation precision is highest, while a value of 0.5 indicates that the evaluation is worthless [105]. The ROC curves of six different feature combination models are shown in Fig. 11. The area under the ROC curve that corresponds to of the
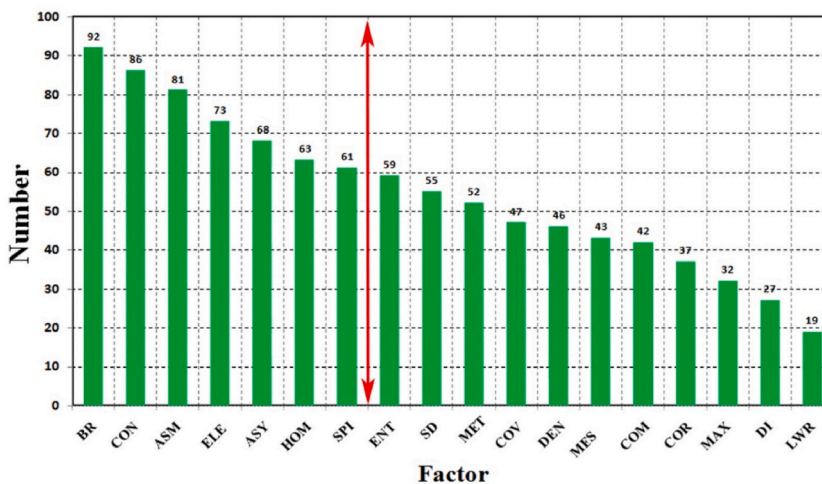

Fig. 9. Attribute reduction set. The number represents the frequency of the feature, and the red line represents the feature set of the segment selection. The features include MAX, MES, SD, and BRof spectral features. MET, VA, HOM, CON, DI, ENT, ASM, and COR of texture features, LWR, SPI, DEN, COM, ASY, ELE and REC of geometry features.
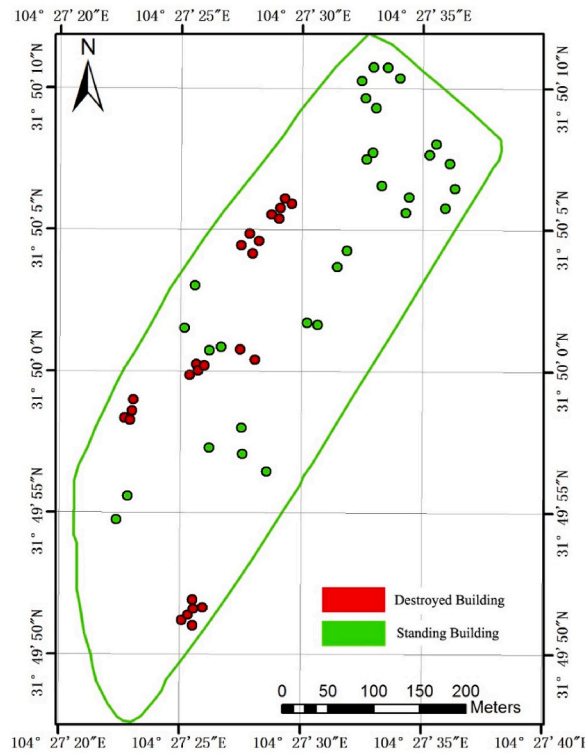
Fig. 10. Distribution of samples in the logistic regression.

Table 3
Logistic regression results and coefficient values used for this study.

Variable	B	S.E.	Wald	Exp(B)	Sig.
BR	1.093	0.135	64.49	2.983	0.000
CON	0.419	0.107	14.32	1.520	0.000
ASM	0.027	0.120	0.050	1.027	0.000
ELE	0.076	0.031	5.98	1.078	0.000
ASY	0.183	0.248	0.494	1.200	0.015
HOM	0.960	0.231	17.02	2.611	0.000
SPI	0.868	0.104	68.82	2.382	0.030

Table 4
Overall statistics of the LRM.

Mode	−2 Log-likelihood	Cox and Snell R Square	Hosmer-Lemeshow Chi-square
DSM	6491.077	0.509	15.001
SAR	6328.167	0.496	18.926
Optical	6309.297	0.484	15.324
SAR + DSM	6970.789	0.571	13.151
Optical + DSM	6869.043	0.535	14.746
Optical + SAR	6682.480	0.526	14.003
Optical + SAR + DSM	7070.968	0.592	13.085

combination of optical image, SAR image, and DSM image is 0.827, which is also the highest among the six types of feature combination models. From the curves we can see that the result that considers the multi-source remote sensing images is better than the results of single image. The evaluation of the combined SAR image and optical image came second. The extraction accuracy using single DSM image is the lowest.

(2) Classification accuracy comparison

Twenty-nine intact buildings and six destroyed buildings were chosen to test the accuracy of the model. The evaluation results of
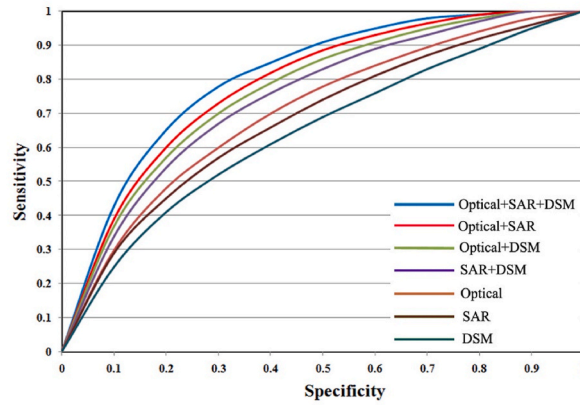
Fig. 11. Receiver operating characteristic (ROC) curve.

different features (Fig. 12(a)) are compared with the results of the field survey (Fig. 12(b)), and then, the evaluation accuracy is analyzed. Table 5 presents the accuracy evaluation results of the earthquake damage extraction for different data sources. Producer's accuracy (PA) represents the probability that the ground truth reference data of this category will be correctly classified in this classification. User's accuracy (UA) represents the ratio of correctly classified checkpoints on the classification map that fall on that category in this classification. Overall Accuracy represents the percentage of inspection points for all correctly classified building categories compared to the total number of inspection points extracted. Half of the destroyed buildings are mistaken for intact buildings in the process of calculating the DSM image, while for the combinations of the optical image and SAR image and the optical image and DSM image, the false identification of destroyed buildings is reduced, and the overall accuracy is 85.71 % and 88.57 %, respectively. For the combination of the SAR image and optical image, the destroyed buildings are easily identified; the overall classification accuracy is 91.43 %, which illustrates that the combination of texture features and geometric features can better identify damaged buildings. Combining the three different sources of data, only one destroyed building is misclassified as an intact building. In addition, one intact building is misclassified as a destroyed building; thus, the overall classification accuracy is 94.2 %, which illustrates that the combination of multi-source data can effectively improve the classification accuracy of earthquake-damaged
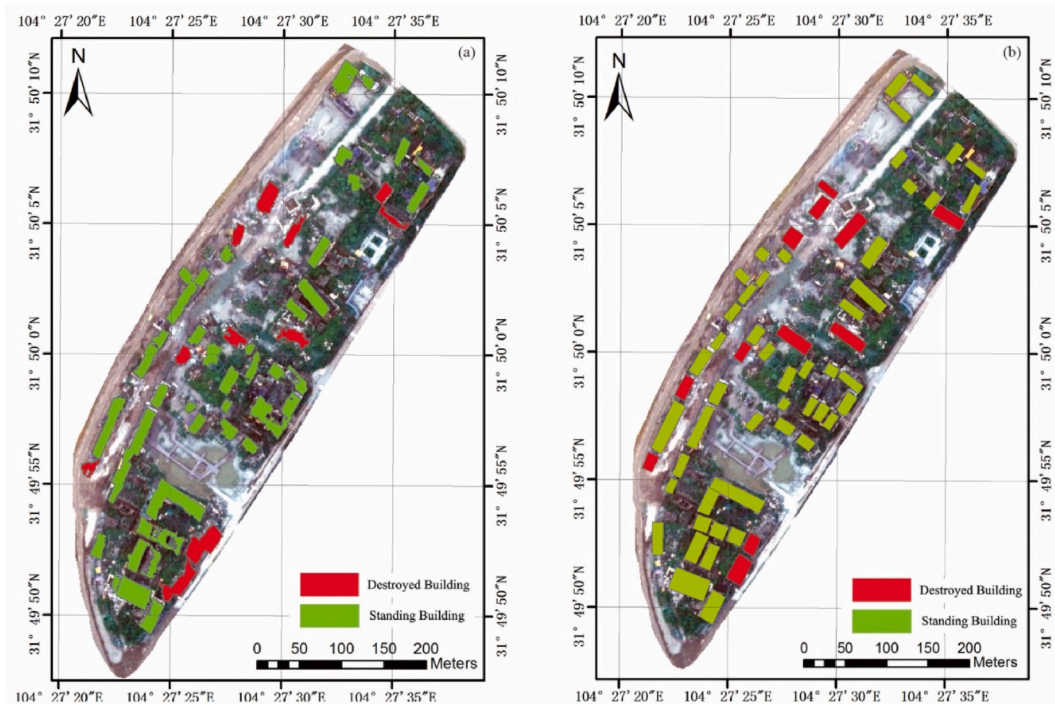

Fig. 12. Experimental results and field investigation results of earthquake-damaged buildings: (a) earthquake-damaged building map based on the logistic regression and (b) earthquake-damaged building map based on high-resolution optical image interpretation and field investigation.

Table 5

Assessment results with different combination modes (Pa=Producer's accuracy; Ua = User's accuracy; UA= Overall accuracy).

Method	Destroyed Building		Intact Building		Overall
	PA	UA	PA	UA	
DSM	42.86	50.00	89.29	86.21	80.00
SAR	46.15	100.00	100.00	75.86	80.00
Optical	57.14	66.67	92.86	89.66	85.71
SAR + DSM	57.14	66.67	92.86	89.66	85.71
Optical + DSM	62.50	83.33	96.30	89.66	88.57
Optical + SAR	66.67	100.00	100.00	89.66	91.43
Optical + SAR + DSM	83.33	83.33	96.55	96.55	94.2.0

information. This also verifies that this method can effectively extract the information of earthquake damaged buildings after obtaining different types of remote sensing data. If there are clouds in the optical image, SAR image and LiDARimage can also be effectively combined to obtain high-precision building distribution information. Generally speaking, the higher the spatial resolution of the image, the higher the accuracy of information recognition. In this paper, the spatial resolution difference of images is not big. If the resolution difference of two or three types of data after earthquake is large, the data with lower resolution can be discarded and the image with higher resolution can be used to build a model, which can also realize the identification of earthquake damaged buildings.

5.4. Discussion

In the experiment, 18 characteristics of spectral features, texture features, and shape features are selected for analysis, and their ability to characterize the earthquake damage of buildings is calculated based on rough set theory. Although three kinds of features can be extracted by optical image or SAR image, the amount of information contained by different data varies. Compared with the optical image, the SAR image has less spectral performance, but the texture information is relatively abundant, and the fusion of multi-source and multi-feature data can compensate for the deficiencies in a single data source.

The logistic method proposed in our experiment is mainly used to construct a prediction model. The method is based on the influence of multiple factors on a certain event, and the probability of model prediction is established. In this paper, the model is applied for the extraction of intact buildings and destroyed buildings after an earthquake. The model establishes a quantitative relationship between the EDAI and different features. During model construction, the division of the model calculation unit is the basis of evaluation. The usual method of unit computation is the grid element partition of the raster data structure. In this study, the object segmented by multiscale segmentation is used as an evaluation unit, which can better describe the characteristics of buildings and express them better by means of evaluation factors.

The validity of the proposed method is verified by using the earthquake site of old Beichuan County as a research area, and the recognition accuracy of the three kinds of data features can reach 94.2 %. In this experiment, data from the Beichuan earthquake site were used; additionally, the site was renovated, and the buildings were cleaned up after the earthquake. The buildings are divided into intact buildings and destroyed buildings, which are limited by the distribution of the earthquake site buildings in old Beichuan County. The method proposed in this paper is based on the sample, and the EDAI can classify earthquake-damaged buildings in detail if a more detailed classification system of seismic damage can be obtained.

6. Conclusions

In this paper, a new method for the quantitative evaluation of earthquake damage to buildings based on multi-source remote sensing data is proposed. This model achieves the evaluation of buildings with different degrees of damage by defining the quantitative relationship between the earthquake damage assessment index and image features. This is the first attempt to fuse different types of image features in the form of models to extract earthquake damaged buildings. The work provides several steps for addressing the problem, including image processing, feature performance evaluation, and the determination of the advantages of multi-source remote sensing in the damage extraction field. Moreover, it defines the possible weights and roles of different features for earthquake damage identification, which raises some difficulties when the features are applied to image classification. The work provides a reference for extracting damaged buildings after obtaining different types of images at different time periods after the earthquake.

The effectiveness of the proposed approach was confirmed using multi-source remote sensing images of old Beichuan County. We tested the method using optical images, SAR images, DSM images, and combined images to demonstrate the effectiveness of the proposed method. By comparing with the results of on-site investigations, the extraction accuracy is 94.2 %, and the area under the ROC curve of the model is 0.827. Model and accuracy verification show that the model has high reliability and accuracy and can be used for the earthquake damaged building assessment. If there are new data sources in the future, this method can also be used to construct models and evaluate seismic damage to buildings.

Data availability statement

Some or all data, models, or code generated or used during the study are available from the corresponding author by request.

Requests may be sent to: liqiang08@163.com.

CRediT authorship contribution statement

Qiang Li: Writing – original draft, Conceptualization. **Jingfa Zhang:** Writing – review & editing, Investigation, Formal analysis. **Hongbo Jiang:** Writing – review & editing, Validation, Methodology.

Declaration of competing interest

The authors declare no conflict of interest.

Acknowledgements

References

[1] Alpaslan Zerdem, G. Rufini, L'Aquila's reconstruction challenges has Italy learned from its previous earthquake disasters, Disasters 37 (1) (2012) 119–143, https://doi.org/10.1111/j.1467-7717.2012.01296.x.

[2] L. Chih-Heng, N. Chuen-Fa, C. Chung-Pai, et al., Coherence difference analysis of Sentinel-1 SAR Interferogram to identify earthquake-induced disasters in urban areas, Rem. Sens. 10 (8) (2018) 1318, https://doi.org/10.3390/rs10081318.

[3] D. Dreger, A. Kaverina, Seismic remote sensing for the earthquake source process and near-source strong shaking A case study of the October 16, 1999 Hector Mine earthquake, Geophys. Res. Lett. 27 (13) (2000) 1941–1944, https://doi.org/10.1029/1999GL011245.

[4] D.M. Tralli, R.G. Blom, V. Zlotnicki, et al., Satellite remote sensing of earthquake, volcano, flood, landslide and coastal inundation hazards, ISPRS J. Photogrammetry Remote Sens. 59 (4) (2005) 185–198, https://doi.org/10.1016/j.isprsjprs.2005.02.002.

[5] F. Dell'Acqua, P. Gamba, Remote sensing and earthquake damage assessment Experiences, limits, perspectives, Proc. IEEE 100 (10) (2012) 2876–2890, https://doi.org/10.1109/JPROC.2012.2196404.

[6] R.J. Ma, Studies on the criteria of post-earthquake building safety evaluation based on principle "repairable level under moderate earthquake", Adv. Mater. Res. 368–373 (2011) 1509–1512, https://doi.org/10.4028/www.scientific.net/AMR.

[7] J.D. Marshall, K. Jaiswal, N. Gould, et al., Post-earthquake building safety inspection lessons from the canterbury, New Zealand, earthquakes, Earthq. Spectra 29 (3) (2013) 1091–1107, https://doi.org/10.1193/1.400015.

[8] D. Brunner, G. Lemoine, L. Bruzzone, Earthquake damage assessment of buildings using VHR optical and SAR imagery, IEEE Trans. Geosci. Rem. Sens. 48 (5) (2010) 2403–2420, https://doi.org/10.1109/TGRS.2009.2038274.

[9] C. Gei, Ck H. Taubenb, Remote sensing contributing to assess earthquake risk from a literature review towards a roadmap, Nat. Hazards 68 (1) (2013) 7–48, https://doi.org/10.1007/s11069-012-0322-2.

[10] M.A. Kader, I.A Jahan, review of the application of remote sensing technologies in earthquake disaster management potentialities and challenges, in: International Conference on Disaster Risk Management, At: BUET, Dhaka, Bangladesh, 2019, pp. 1–6. January12-14.

[11] E. Can, Ku Senol, M.E. Kartal, Effects of mining subsidence on masonry buildings in Zonguldak hard coal region in Turkey, Environ. Earth Sci. 66 (8) (2012) 2503–2518, https://doi.org/10.1007/s12665-011-1473-2,2012.

[12] J. Yeom, M. Jung, Y. Kim, Detecting damaged building parts in earthquake-damaged areas using differential seeded region growing, Int. J. Rem. Sens. 38 (3–4) (2017) 985–1005, https://doi.org/10.1080/01431161.2016.1274445.

[13] M. Butenuth, D. Frey, A. Nielsen, H. Skriver, Infrastructure assessment for disaster management using multi-sensor and multi-temporal remote sensing imagery, Int. J. Rem. Sens. 32 (2011) 8575–8594, https://doi.org/10.1080/01431161.2010.542204.

[14] M. Chini, L. Pulvirenti, N. Pierdicca, Analysis and interpretation of the COSMO-SkyMed observations of the 2011 Japan tsunami, Geosci. Rem. Sens. Lett. IEEE 9 (2012) 467–471, https://doi.org/10.1109/LGRS.2011.2182495.

[15] T.L. Wang, Y.Q. Jin, Post-earthquake building damage assessment using multimutual information from pre-event optical image and post-event SAR image, Geosci. Rem. Sens. Lett. IEEE 9 (3) (2012) 452–456, https://doi.org/10.1109/LGRS.2011.2170657.

[16] P. Gamba, F. Casciati, GIS and image understanding for near-real-time earthquake damage assessment: remote sensing and GIS for hazards, Photogramm. Eng. Rem. Sens. 64 (1998) 987–994, https://doi.org/10.1117/1.482668.

[17] N. Ogawa, F. Yamazaki, Photo-interpretation of building damage due to earthquakes using aerial photographs, Proceedings of the 12th world conference on earthquake engineering (1906) 2000.

[18] C. Yonezawa, S. Takeuchi, Decorrelation of SAR data by urban damages caused by the 1995 Hyogoken-nanbu earthquake, Int. J. Rem. Sens. 22 (8) (2001) 1585–1600, https://doi.org/10.1080/01431160118187.

[19] M. Turker, B.T. San, Detection of collapsed buildings caused by the 1999 Izmit, Turkey earthquake through digital analysis of post-event aerial photographs, Int. J. Rem. Sens. 25 (21) (2004) 4701–4714, https://doi.org/10.1080/01431160410001709976.

[20] S. Stramondo, C. Bignami, M. Chini, et al., Satellite radar and optical remote sensing for earthquake damage detection results from different case studies, Int. J. Rem. Sens. 27 (20) (2006) 4433–4447, https://doi.org/10.1080/01431160600675895.

[21] D. Brunner, G. Lemoine, L. Bruzzone, Earthquake damage assessment of buildings using VHR optical and SAR imagery, IEEE Trans. Geosci. Rem. Sens. 48 (5) (2010) 2403–2420, https://doi.org/10.1109/TGRS.2009.2038274.

[22] K. Zhang, S.C. Chen, D. Whitman, et al., A progressive morphological filter for removing nonground measurements from airborne LIDAR data, Geoscience and Remote Sensing, IEEE Transactions on 41 (4) (2003) 872–882, https://doi.org/10.1109/TGRS.2003.810682.

[23] M. Sakamoto, Y. Takasago, K. Uto, et al., Automatic detection of damaged area of Iran earthquake by high-resolution satellite imagery, Geoscience and Remote Sensing Symposium, 2004. IGARSS'04. Proceedings. 2004 IEEE International. IEEE 2 (2004) 1418–1421, https://doi.org/10.1109/IGARSS.2004.1368685.

[24] K. Saito, R.J.S. Spence, C. Going, et al., Using high-resolution satellite images for post-earthquake building damage assessment a study following the 26 January 2001 Gujarat earthquake, Earthq. Spectra 20 (1) (2004) 145–169, https://doi.org/10.1193/1.1650865.

[25] M. Kohiyama, F. Yamazaki, Damage detection for 2003 Bam, Iran, earthquake using Terra-ASTER satellite imagery, Earthq. Spectra 21 (S1) (2005) 267–274, https://doi.org/10.1193/1.2098947.

[26] E.M. Rathje, M. Crawford, K. Woo, et al., Damage patterns from satellite images of the 2003 Bam, Iran, Earthquake, Earthq. Spectra 21 (S1) (2005) 295–307, https://doi.org/10.1193/1.2101047.

[27] E.M. Rathje, K.S. Woo, M. Crawford, et al., Earthquake damage identification using multi-temporal high-resolution optical satellite imagery, Geoscience and Remote Sensing Symposium, 2005. IGARSS'05. Proceedings. 2005 IEEE International. IEEE 7 (2005) 5045–5048, https://doi.org/10.1109/IGARSS.2005.1526812.

[28] L. Gusella, B.J. Adams, G. Bitelli, et al., Object-oriented image understanding and post-earthquake damage assessment for the 2003 Bam, Iran, earthquake, Earthq. Spectra 21 (S1) (2005) 225–238, https://doi.org/10.1193/1.2098629.

[29] T.T. Vu, M. Matsuoka, F. Yamazaki, Detection and animation of damage using very high-resolution satellite data following the 2003 Bam, Iran, earthquake, Earthq. Spectra 21 (S1) (2005) 319–327, https://doi.org/10.1193/1.2101127.

[30] S. Stramondo, C. Bignami, M. Chini, et al., Satellite radar and optical remote sensing for earthquake damage detection results from different case studies, Int. J. Rem. Sens. 27 (20) (2006) 4433–4447, https://doi.org/10.1080/01431160600675895.

[31] J. Hoffmann, Mapping damage during the Bam (Iran) earthquake using interferometric coherence, Int. J. Rem. Sens. 28 (6) (2007) 1199–1216, https://doi.org/10.1080/01431160600928567.

[32] P. Gamba, F. Dell'Acqua, G. Trianni, Rapid damage detection in the Bam area using multitemporal SAR and exploiting ancillary data, IEEE Trans. Geosci. Rem. Sens. 45 (6) (2007) 1582–1589, https://doi.org/10.1109/TGRS.2006.885392.

[33] A.L. Chesnel, R. Binet, L. Wald, Object oriented assessment of damage due to natural disaster using very high resolution images, Geoscience and Remote Sensing Symposium, 2007. IGARSS 2007. IEEE International. IEEE (2007) 3736–3739, https://doi.org/10.1109/IGARSS.2007.4423655.

[34] F. Samadzadegan, H. Rastiveisi, Automatic detection and classification of damaged buildings, using high resolution satellite imagery and vector data, Int. Arch. Photogram. Rem. Sens. Spatial Inf. Sci. 37 (2008) 415–420.

[35] D. Brunner, G. Lemoine, L. Bruzzone, Earthquake damage assessment of buildings using VHR optical and SAR imagery, IEEE Trans. Geosci. Rem. Sens. 48 (5) (2010) 2403–2420, https://doi.org/10.1109/TGRS.2009.2038274.

[36] T.T. Vu, M. Matsuoka, F. Yamazaki, Shadow analysis in assisting damage detection due to earthquakes from QuickBird imagery, Proceedings of the 10th international society for photogrammetry and remote sensing congress (2004) 607–611.

[37] F. Yamazaki, K. Kouchi, M. Matsuoka, et al., Damage detection from high-resolution satellite images for the 2003 Boumerdes, Algeria earthquake, 13th World Conference on Earthquake Engineering, International Association for Earthquake Engineering, Vancouver, British Columbia, Canada 13 (2004).

[38] G. Bitelli, R. Camassi, L. Gusella, et al., Image Change Detection on Urban Area the Earthquake Case, XXth ISPRS Congress, Istanbul, Turkey, 2004, p. 692.

[39] G. Trianni, P. Gamba, Damage detection from SAR imagery application to the 2003 Algeria and 2007 Peru earthquakes, International Journal of Navigation and Observation 2008 (2008), https://doi.org/10.1155/2008/762378.

[40] M. Chini, C. Bignami, S. Stramondo, et al., Uplift and subsidence due to the 26 December 2004 Indonesian earthquake detected by SAR data, Int. J. Rem. Sens. 29 (13) (2008) 3891–3910, https://doi.org/10.1080/01431160701871112.

[41] M. Chini, F.R. Cinti, S. Stramondo, Co-seismic surface effects from very high resolution panchromatic images the case of the 2005 Kashmir (Pakistan) earthquake, Nat. Hazards Earth Syst. Sci. 11 (3) (2011) 931–943, https://doi.org/10.5194/nhess-11-931-2011.

[42] M. Matsuoka, F. Yamazaki, Use of SAR imagery for monitoring areas damaged due to the 2006 Mid Java, Indonesia earthquake, Proceedings of 4th international workshop on remote sensing for post-disaster response, 2006, pp. 1–5.

[43] H. Miura, F. Yamazaki, M. Matsuoka, Identification of damaged areas due to the 2006 Central Java, Indonesia earthquake using satellite optical images, Urban Remote Sensing Joint Event, 2007. IEEE (2007) 1–5, https://doi.org/10.1109/URS.2007.371867.

[44] F. Yamazaki, T.T. Vu, M. Matsuoka, Context-based detection of post-disaster damaged buildings in urban areas from satellite images, Urban Remote Sensing Joint Event, 2007. IEEE (2007) 1–5, https://doi.org/10.1109/URS.2007.371869.

[45] D. Brunner, G. Lemoine, L. Bruzzone, Earthquake damage assessment of buildings using VHR optical and SAR imagery, IEEE Trans. Geosci. Rem. Sens. 48 (5) (2010) 2403–2420, https://doi.org/10.1109/TGRS.2009.2038274.

[46] G. Trianni, P. Gamba, Damage detection from SAR imagery application to the 2003 Algeria and 2007 Peru earthquakes, International Journal of Navigation and Observation 2008 (2008), https://doi.org/10.1155/2008/762378.

[47] H.D. Guo, L.L. Lu, J.W. Ma, et al., An improved automatic detection method for earthquake-collapsed buildings from ADS40 image, Chin. Sci. Bull. 54 (18) (2009) 3303–3307, https://doi.org/10.1007/s11434-009-0461-3.

[48] Y.H. Liu, C.Y. Qu, X.J. Shan, et al., Application of SAR data to damage identification of the Wenchuan earthquake, Acta Seismologica Sinica 32 (2) (2010) 214–223, https://doi.org/10.3969/j.issn.0253-3782.2010.02.009.

[49] T.T. Vu, Y. Ban, Context-based mapping of damaged buildings from high-resolution optical satellite images, Int. J. Rem. Sens. 31 (13) (2010) 3411–3425, https://doi.org/10.1080/01431161003727697.

[50] F. Duan, H. Gong, W. Zhao, Collapsed houses automatic identification based on texture changes of post-earthquake aerial remote sensing image, Geoinformatics, 2010 18th International Conference on. IEEE (2010) 1–5, https://doi.org/10.1109/GEOINFORMATICS.2010.5567622.

[51] T. Balz, M. Liao, Building-damage detection using post-seismic high-resolution SAR satellite data, Int. J. Rem. Sens. 31 (13) (2010) 3369–3391, https://doi.org/10.1080/01431161003727671.

[52] G. Pan, D. Tang, Damage information derived from multi-sensor data of the Wenchuan Earthquake of May 2008, Int. J. Rem. Sens. 31 (13) (2010) 3509–3519, https://doi.org/10.1080/01431161003730865.

[53] Y. Dong, Q. Li, A. Dou, et al., Extracting damages caused by the 2008 Ms 8.0 Wenchuan earthquake from SAR remote sensing data, J. Asian Earth Sci. 40 (4) (2011) 907–914, https://doi.org/10.1016/j.jseaes.2010.07.009.

[54] X. Tong, Z. Hong, S. Liu, et al., Building-damage detection using pre-and post-seismic high-resolution satellite stereo imagery a case study of the May 2008 Wenchuan earthquake, ISPRS J. Photogrammetry Remote Sens. 68 (2012) 13–27, https://doi.org/10.1016/j.isprsjprs.2011.12.004.

[55] J. Ma, S. Qin, Automatic depicting algorithm of earthquake collapsed buildings with airborne high resolution image, Geoscience and Remote Sensing Symposium (IGARSS), 2012 IEEE International. IEEE (2012) 939–942, https://doi.org/10.1109/igarss.2012.6351400.

[56] R. Guida, A. Iodice, D. Riccio, Monitoring of collapsed built-up areas with high resolution SAR images, Geoscience and Remote Sensing Symposium (IGARSS), 2010 IEEE International. IEEE (2010) 2422–2425, https://doi.org/10.1109/IGARSS.2010.5650083.

[57] D. Polli, F. Dell'Acqua, P. Gamba, et al., Earthquake damage assessment from post-event only radar satellite data, Proceedings of the eighth international workshop on remote sensing for disaster response 30 (2010).

[58] F. Dell'Acqua, D.A. Polli, Post-event only VHR radar satellite data for automated damage assessment, Photogramm. Eng. Rem. Sens. 77 (10) (2011) 1037–1043, https://doi.org/10.1111/j.1467-9671.2011.01286.x.

[59] M. Gerke, N. Kerle, Automatic structural seismic damage assessment with airborne oblique Pictometry imagery, Photogramm. Eng. Rem. Sens. 77 (9) (2011) 885–898, https://doi.org/10.14358/PERS.77.9.885.

[60] E.S. Malinverni, Change detection applying landscape metrics on high remote sensing images, Photogramm. Eng. Rem. Sens. 77 (10) (2011) 1045–1056, https://doi.org/10.14358/pers.77.10.1045.

[61] E. Hussain, S. Ural, K.H. Kim, et al., Building extraction and rubble mapping for city port-au-prince post-2010 earthquake with GeoEye-1 imagery and lidar data, Photogramm. Eng. Rem. Sens. 77 (10) (2011) 1011–1023. DOI:info:DOI/10.14358/PERS.77.10.1011.

[62] H. Miura, S. Modorikawa, S.H. Chen, Texture characteristics of high-resolution satellite images in damaged areas of the 2010 Haiti earthquake, Proceedings of 9th International Workshop on Remote Sensing for Disaster Response (2011) 1–9.

[63] P. Uprety, F. Yamazaki, Use of high-resolution SAR intensity images for damage detection from the 2010 Haiti earthquake, Geoscience and Remote Sensing Symposium (IGARSS), 2012 IEEE International. IEEE (2012) 6829–6832, https://doi.org/10.1109/IGARSS.2012.6352595.

[64] M. Satake, T. Kobayashi, J. Uemoto, et al., Damage estimation of the great east Japan earthquake with airborne SAR (Pi-SAR2) data, Geoscience and Remote Sensing Symposium (IGARSS), 2012 IEEE International. IEEE (2012) 1190–1191, https://doi.org/10.1117/12.977613.

[65] W. Liu, F. Yamazaki, H. Gokon, et al., Extraction of damaged buildings due to the 2011 Tohoku, Japan earthquake tsunami, Geoscience and Remote Sensing Symposium (IGARSS), 2012 IEEE International. IEEE (2012) 4038–4041, https://doi.org/10.1109/IGARSS.2012.6350523.

[66] M. Rehor, T. Voegtle, Improvement of building damage detection and classification based on laser scanning data by integrating spectral information, International Archive of Photogrammetry and Remote Sensing 37 (B7) (2018) 1599–1605, 2018.

[67] H. Yu, G. Cheng, X. Ge, Earthquake-collapsed building extraction from LiDAR and aero photograph based on OBIA, In the 2nd International Conference on Information Science and Engineering (ICISE), IEEE (2011) 2034–2037, https://doi.org/10.1109/ICISE.2010.5691203.

[68] E. Hussain, S. Ural, K. Kim, C.S. Fu, J. Shan, Building extraction and rubble mapping for city of Port-Au-Prince post-2010 earthquake with GeoEye-1 imagery and Lidar data, Photogramm. Eng. Rem. Sens. 77 (10) (2011) 1011–1023, https://doi.org/10.14358/PERS.77.10.1011.

[69] J.F. Zhang, Multi-source remote sensing data fusion status and trends, International Journal of Image and Data Fusion 1 (2010) 5–24, https://doi.org/10.1080/19479830903561035.

[70] Y. Du, F. Xie, Z. Wang, Wenchuan earthquake surface fault rupture and disaster A lesson on seismic hazard assessment and mitigation, International Journal of Geophysics 9 (11) (2012) 1–6, https://doi.org/10.1155/2012/974763.

[71] G.L. Wang, Z. Jun-Hui, L. Hong-Shuai, Investigation and preliminary analysis of geologic disasters in Beichuan county induced by Wenchuan Earthquake, Chin. J. Geol. Hazard Control 3 (2009) 47–51 (In Chinese).

[72] L.X. Gong, C. Wang, F. Wu, J.F. Zhang, H. Zhang, Q. Li, Earthquake-induced building damage detection with post-event sub-meter vhr terrasar-x staring spotlight imagery, Rem. Sens. 8 (12) (2016) 817, https://doi.org/10.3390/rs8110887.

[73] C. Schweier, M. Markus, Classification of collapsed buildings for fast damage and loss assessment, Bull. Earthq. Eng. 4 (2) (2006) 177–192, https://doi.org/10.1007/s10518-006-9005-2.

[74] Ph Hartl, F. Cheng, Delimiting the building heights in a city from the shadow on a panchromatic spot-image part 2 test of a complete city, Int. J. Rem. Sens. (1995), https://doi.org/10.1080/01431169508954594.

[75] F. Yamazaki, Y. Iwasaki, W. Liu, et al., Detection of damage to building side-walls in the 2011 Tohoku, Japan earthquake using high-resolution TerraSAR-X images, Proc. SPIE-Int. Soc. Opt. Eng. 8892 (2013) 12, https://doi.org/10.1117/12.2029465.

[76] H. Miura, S. Midorikawa, Distribution of building damage in the southeastern part of beichuan county by the 2008 sichuan, China, earthquake based on visual detection of satellite optical images, Journal of Japan Association for Earthquake Engineering 10 (3) (2011) 46–57, https://doi.org/10.5610/jaee.10.3_46.

[77] Ferro, A, Brunner, D, Bruzzone, L. On the relationship between double bounce and the orientation of buildings in VHR SAR images. Geoscience and Remote Sensing Letters, IEEE2011, 8(4) :612-616. DOI:10.1109/LGRS.2010.2097580.

[78] Dominik Brunner, Lorenzo Bruzzone, Adamo Ferro, Fortuny Guasch Joaquim, Guido Lemoine, Analysis of the double bounce scattering mechanism of buildings in VHR SAR data, Proc. SPIE-Int. Soc. Opt. Eng. (2008) 7109, https://doi.org/10.1117/12.801670.

[79] Z. Jun, X.L. Ding, Z.W. Li, High-rise building layover exploitation with non-local frequency estimation in SAR interferograms, Rem. Sens. 9 (6) (2017) 579, https://doi.org/10.3390/rs9060579.

[80] V. Pérez-Gracia, O. Caselles, J. Clapés, R. Osorio, J. Canas, Apujades, G. L, Radar exploration applied to historical buildings a case study of the marques de llió palace, in barcelona (spain), Eng. Fail. Anal. 16 (7) (2009) 1039–1050, https://doi.org/10.1016/j.engfailanal.2008.05.007.

[81] L. Guido, C. Michele, Enric Fernández, Radar interferometry for monitoring the vibration characteristics of buildings and Civil structures recent case studies in Spain, Sensors 17 (4) (2017) 669, https://doi.org/10.3390/s17040669.

[82] V. Perez-Gracia, S. Santos-Assuncao, O. Caselles, et al., Combining ground penetrating radar and seismic surveys in the assessment of cultural heritage buildings The study of roofs, columns, ground of the gothic church Santa Maria del Mar, in Barcelona (Spain), Struct. Control Health Monit. 26 (4) (2019), https://doi.org/10.1002/stc.2327 e2327.1-e2327.14.

[83] X.Y. Wen, H. Zhang, The high resolution SAR image simulation and analysis of the damaged building in earthquake, Journal of Remote Sensing 1 (2009) 169–176 (In Chinese).

[84] T.T. Vu, M. Matsuoka, F. Yamazaki, LIDAR-based change detection of buildings in dense urban areas, IEEE International Geoscience & Remote Sensing Symposium. IEEE (2004), https://doi.org/10.1109/IGARSS.2004.1370438.

[85] F. Wu, L. Gong, C. Wang, et al., Damage building analysis in TerraSAR-X new staring spotlight mode SAR imagery, 2015 IEEE 5th Asia-Pacific Conference on Synthetic Aperture Radar (APSAR). IEEE (2015), https://doi.org/10.1109/APSAR.2015.7306220.

[86] L.C. Chen, T. Teo, A. Kuo, Y. C, et al., Shaping polyhedral buildings by the fusion of vector maps and lidar point clouds, Photogramm. Eng. Rem. Sens. 74 (9) (2015) 1147–1157, https://doi.org/10.14358/pers.73.9.1147.

[87] Infoterra, Radiometric Calibration of TerraSAR-X Data Beat Nought and Sigma Nought Coefficient, Calculation (2008) 1–15.

[88] F.J. Zhao, Research on disaster information extraction technology using remote sensing image, Institute of engineering mechanics China Earthquake Administration (2010) 61–87.

[89] R.M. Haralick, K. Shanmugan, I. Dinstein, Texture features for image classification, IEEE Transactions on Systems, Man and Cybernetics 3 (1973) 610–621, 1973.

[90] E.M. Wood, A.M. Pidgeon, V.C. Radeloff, N.S. Keuler, Image texture as a remotely sensed measure of vegetation structure, Remote Sensing of Environment 121 (2012) 516–526, https://doi.org/10.1111/j.1600-0587.2008.05512.x.

[91] Q.H. Chen, Research and Realization of Multi-Sources Remote Sensing Data on Object Oriented, China University of Geosciences, Wuhan, 2007 (In Chinese).

[92] Z. Pawlak, Rough Sets Theoretical Aspects of Reasoning about Data, Kluwer Academic Publishers, Netherlands, 1991.

[93] S. Ramanna, J.F. Peters, T. Ahn, Software quality knowledge discovery a rough set approach, International Computer Software and Applications Conference on Prolonging Software Life Development and Redevelopment. IEEE Computer Society (2002) 1140–1145.

[94] W.T. Chen, Y.T. Qian, Network intrusion detection method based on rough set theory, Comput. Eng. 32 (16) (2006) 132–135 (In Chinese).

[95] B. Zheng, Y.X. Jin, Analysis on factors leading to human fault in marine accidents based on attribute reduction, J. Shanghai Marit. Univ. 31 (1) (2010) 91–94 (In Chinese).

[96] Definiens Image Company, eCognition User Guide, 2004. German.

[97] D.W. Hosmer, S. Lemeshow, Applied Logistic Regression, Wiley, New York, 1989, https://doi.org/10.1002/9781118548387.

[98] J.C. Wang, Z.G. Guo, Logistic Regression Model Method and Application, Higher Education Press, Beijing, 2001 (In Chinese).

[99] S. Chauhan, M. Sharma, M.K. Arora, Landslide susceptibility zonation of the Chamoli region, Garhwal Himalayas, using logistic regression model, Landslides 7 (4) (2010) 411–423, https://doi.org/10.1007/s10346-010-0202-3.

[100] Jasmit SureshKumar Shah, An Adaptive Ensemble Learner Function via Bagging and Rank Aggregation with Applications to High Dimensional Data, Dissertations & Theses - Gradworks, 2011, https://doi.org/10.18297/etd/1306.

[101] G.F. Ficetola, E. Padoa-Schioppa, A. Monti, RDe Massa, F. Bernardi, L. Bottoni, The importance of aquatic and terrestrial habitat for the European pond turtle (Emys orbicularis) implications for conservation planning and management, Rev. Canad. Zool. 82 (11) (2004) 1704–1712, https://doi.org/10.1139/z04-170; [101a] S. Menard, Applied Logistic Regression Analysis, Sage Publications, California, 1995.

[102] W.A. Clark, P.L. Hosking, Statistical Methods for Geographers, John Wiley and Sons, New York, 1986. ISBN: 978-0-471-81807-6.

[103] Qian, X. Nguyen, D. T , Dong, Y.Prognostic Score Predicts Survival in HPV-Negative Head and Neck Squamous Cell Cancer Patients .International journal of biological sciences, 2019, 15(7):1336-1344. DOI:10.7150/ijbs.33329.

[104] M.H. Zweig, G. Campbell, Receiver-operating characteristic (ROC) plots - a fundamental evaluation tool in clinical medicine, Clin. Chem. 39 (1993) 561–577, https://doi.org/10.1093/clinchem/39.4.561.

[105] A. Lulseged, Y. Hiromit, The application of GIS-based logistic regression for landslide susceptibility mapping in the Kakuda-Yahiko Mountains, Central Japan, Geomorphology 65 (2005) 15–31, https://doi.org/10.1016/j.geomorph.2004.06.010.

List of Abbreviations

MAX: Maximum
SD: standard deviation
MES: mean value of spectral features
BR: brightness
MET: mean value of texture features

VA: variance
HOM: homogeneity
DI: dissimilarity
ENT: entropy
ASM: angular second moment
CON: contrast
COR: correlation
LWR: length-width ratio
SPI: shape index
DEN: density
ASY: asymmetry
REC: rectangularity
ELE: elevation
ROC: Receiver operating characteristic
Pa: Producer's accuracy
Ua: User's accuracy
UA: Overall accuracy
UAV: unmanned aerial vehicle
DSM: digital surface model
LiDAR: light detection and ranging
EDAI: earthquake damage assessment index
SPSS: Statistical Package of Social Sciences
SAR: synthetic aperture radar
LRM: Logistic regression model